JOURNAL OF GEOPHYSICAL RESEARCH, VOL. 106, NO. C5, PAGES 9223–9240, MAY 15, 2001

Effects of topographic variability on the formation of upwelling centers off New Jersey: A theoretical model

Y. Tony Song

Jet Propulsion Laboratory, California Institute of Technology, Pasadena, California

Dale B. Haidvogel and Scott M. Glenn

Institute of Marine and Coastal Sciences, Rutgers University, New Brunswick, New Jersey

Abstract. A theoretical wind-driven, continuously stratified coastal ocean model with varying topography is developed to examine the formation of upwelling centers in coastal oceans, such as those observed along the New Jersey coast. In this simple model an Ekman transport layer is induced by a wind-driven shear friction profile to force the coastal ocean. An analytical perturbation solution, including a component of internal Kelvin waves, is solved for the coastal upwelling system with weak alongshore-varying topography. Under uniformly upwelling favorable winds, the model solutions show that alongshore-varying topography leads to the formation of upwelling centers along the coast by increasing upwelling on the downslope sides of topographic highs and decreasing upwelling on the upslope sides of topographic highs, similar to the observed features off the New Jersey coast during summer seasons. A conservation theorem is derived that indicates the topographic variation does not change the total amount of upwelled water but redistributes it unevenly along the coast to form enhanced upwelling centers. The theory suggests that alongshore-varying topography plays an important role in controlling the formation of upwelling centers as it enhances upwelling at some locations and induces downwelling at others. In addition, the variations of the upwelling fronts are further complicated by the topographically trapped Kelvin waves.

1. Introduction

Alongshore-varying upwelling fronts have been observed in most of the world's coastal oceans [*Brink*, 1983; *Barth*, 1989]. Recently, observations off the New Jersey coast revealed recurrent upwelling centers developed at some specific locations along the coast [*Glenn et al*., 1996]. Upwelling occurs along the New Jersey coast when winds blow from the southwest, resulting in the offshore transport of warm surface water and the onshore transport of cold bottom water. The upwelling response to the southwesterly winds usually begins as a narrow, fairly uniform cold band along the coast that forms a strong temperature and salinity front along its offshore side. After a few days of persistent winds or relaxing an ~50 km long wavelike pattern develops along the front, and the near-shore band of the upwelling water forms a series of isolated cold surface patches. Each year, these upwelling centers are located offshore of the same inlets and estuaries previously identified as regions of recurrent low dissolved oxygen (DO). Plates 1a–1c are satellite infrared images of typical upwelling events and conductivity-temperature-depth (CTD) transects of the New Jersey coast that occurred during the summers of 1993, 1994, and 1995, respectively.

Upwelling also transports nutrients into the euphotic zone where they can be consumed by phytoplankton. Under the proper circumstances the resulting phytoplankton blooms can affect bottom DO concentrations. For example, *Stoddard et al*. [1986] found that the organic matter produced during a phytoplankton bloom can accumulate below the pycnocline and deplete the bottom DO as it decays. Bottom DO concentrations are saturated at about 6–7 mL L^{-1} in the summer, while hypoxic values below about 3 mL L^{-1} begin to stress benthic organisms. The most severe example of this was the 1976 anoxia (no oxygen) event that affected nearly the entire New Jersey coast and resulted in a $600 million loss to the shellfishing industry [*Figley et al*., 1979]. Recently, observations suggest that locations of the recurrent hypoxia may be related to the development of the recurrent upwelling centers in which nutrients are trapped. The alongshore variation of the bottom topography has been hypothesized to cause the upwelling centers in an idealized numerical model [*Glenn et al*., 1996], but it is not known how topography plays a role in controlling the formation, evolution, and subsequent breakdown of upwelling fronts.

Coastal upwelling on the west coast of the United States has been studied extensively in the past 20 years. For example, using a simple numerical two-layer model, *Peffley and O'Brien* [1976] examined the effects of a ridge off Oregon. Their simulation results suggested that bottom relief may be responsible for the enhanced upwelling and that the alongshore variation of bottom topography is more important than the coastline curvature in causing it. Using the semispectral primitive equation model, *Haidvogel et al*. [1991a] studied the dynamics of the filament formation in the presence of both topography and irregular coastline geometry but in the absence of wind forcing. They conclude that the existence of the cape geometry and the southward surface flow is necessary in the model to produce filament generation. More recently, *Song and Haidvogel* [1993], using the S-Coordinate Rutgers University Model (SCRUM)

Paper number 2000JC000244.
0148-0227/01/2000JC000244$09.00

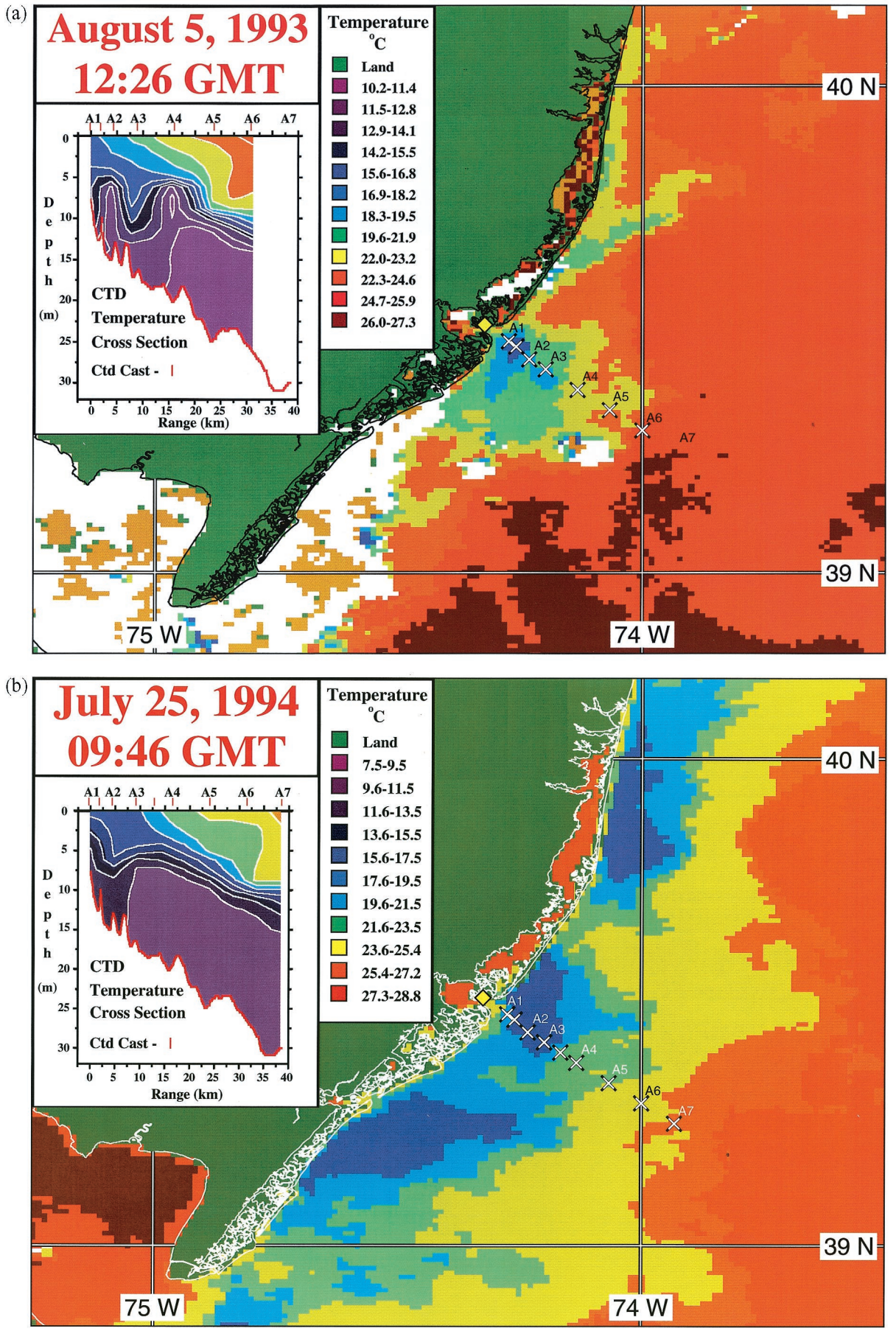

Plate 1. Satellite images of upwelling events along the southern New Jersey coast on (a) August 5, 1993, (b) July 25, 1994, and (c) July 27, 1995. Each image indicates the upwelled surface water has converged into a series three cold patches. CTD transects through the Mullica upwelling center are shown in the upper right corners. (d) New Jersey coastal bathymetry developed from the U.S. Geological Survey 30″ data set. The upwelling centers are located on the northern sides of the topographic highs as indicated by the shaded areas marked by B, C, and D, which were identified as the historical regions of recurrent of low dissolved oxygen.

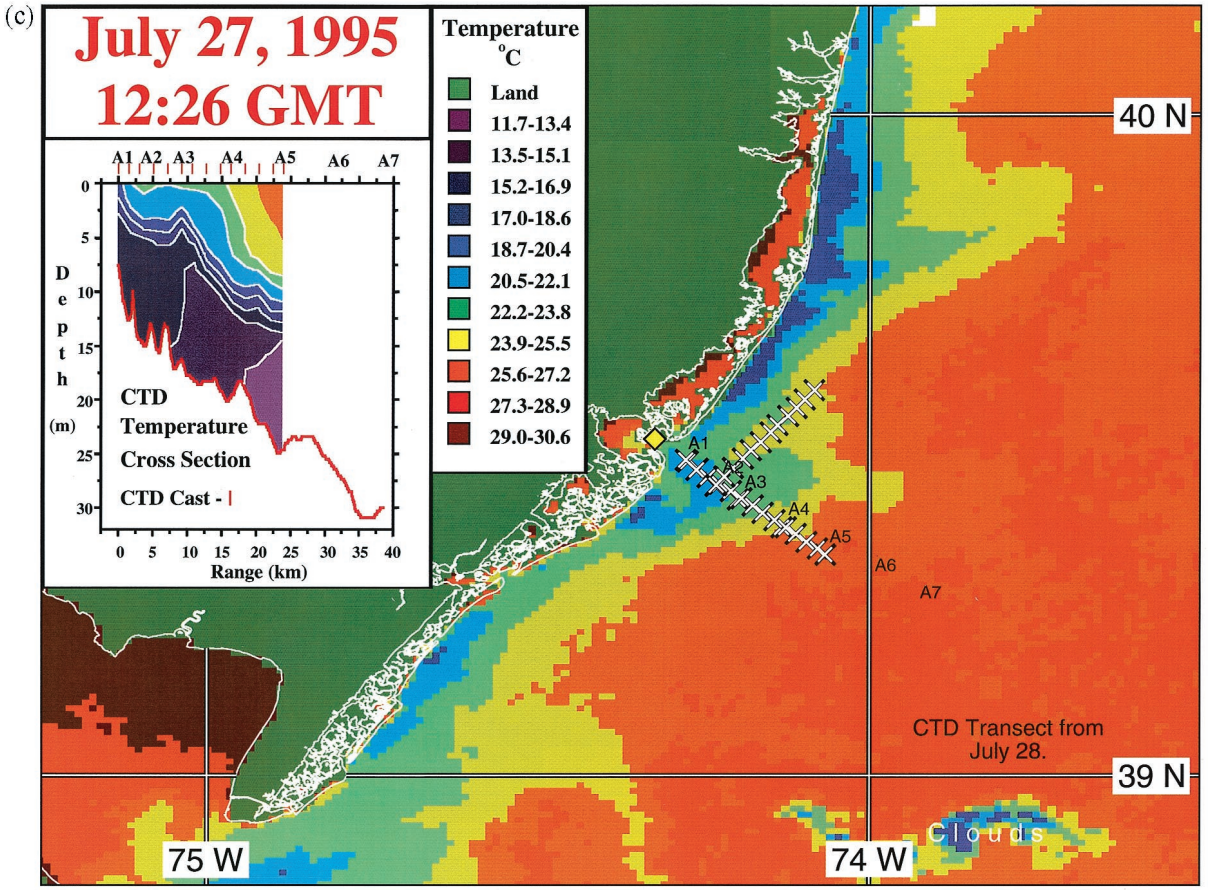

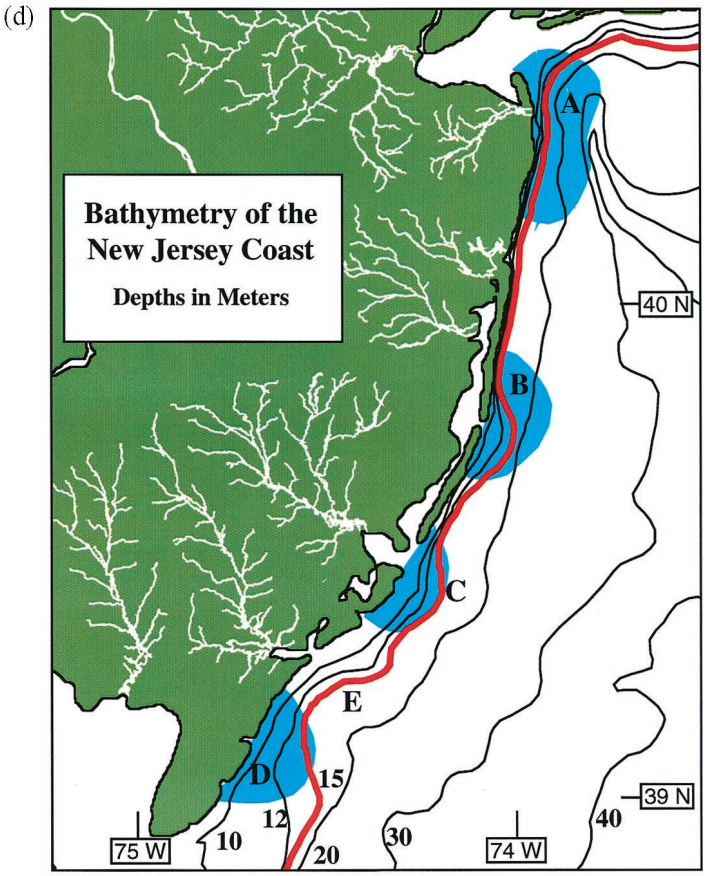

Plate 1. (continued)

[*Song and Haidvogel*, 1994], examined the joint effects of coastal geometry and surface forcing on the California current system. Their results confirmed that the coastal geometry and surface forcing are both important for a better simulation of the upwelling features of the region. However, physical oceans are complex, and numerical models are their approximations. Sometimes, numerical simulations are not sufficient to explain the physical mechanism. Theoretical models, even simple ones, are useful to identify important factors and to gain physical insights of the complex system.

In a simple analytical, uniformly stratified linear model, *Killworth* [1978] has successfully examined the effects of small, slow, alongshore-varying topography on upwelling and internal Kelvin wave propagation. His results revealed a three-dimensional solution with enhanced upwelling on one side of a ridge and downwelling on the other side. A complicated cyclonic and anticyclonic circulation is associated with a shoreward flow over the ridge. He also considered the modification of an internal Kelvin wave by isolated topography, and its energy scattered into vertical modes. However, the Ekman transport layer in his model is represented by a delta function sink of fluid situated at the intersection of the sea surface and the coast, similar to that used by *Pedlosky* [1978a, 1978b]. In *Pedlosky*'s [1978a, 1978b] models the offshore transport of surface water within the Ekman layer is not included in the whole water volume. In fact, upwelling centers and filaments are surface layer features and are important for biological processes [*Moisan and Hofmann*, 1996; *Moisan et al*., 1996]. Without including the Ekman layer in the model it seems not to be suitable for most of the coastal problems, such as the New Jersey coast where all the upwelling activity occurs in water depths of 50 m or less.

The purpose of this study is to develop a theoretical coastal model to understand the mechanism of the formation of upwelling centers and the role of topography in the wind-driven upwelling system. We will extend *Killworth*'s [1978] coastal model to include a surface Ekman transport layer for the shallow shelf region off New Jersey. The paper is organized as follows. In section 2 the theoretical wind-driven, continuously stratified coastal model is developed, and its corresponding pressure equation is derived. In section 3 an upwelling solution with a weak variation of alongshore topography is solved using the perturbation method. A conservation theorem is derived and its implication for the upwelling dynamics is provided. Finally, in section 4 the conclusions are summarized. More details of mathematical procedure for seeking the model solutions are given in Appendixes A and B.

2. Wind-Driven Model

2.1. Model Geometry and Equations

We consider a simple rectangular coastal region with one side as the coastal wall and its opposite side as the offshore boundary. The other two sides of the region represent the cross-shore open boundaries. Similar to that used by *Killworth* [1978], the underlying bottom topography is taken to be

$$h(y) = H - B(y)$$

but with characteristics typical of the wide flat shelf (Plate 1d) off the New Jersey coast. H is the total depth, and $B(y) \geq 0$ is the perturbation of the alongshore topography. The main assumption in this model is that $B(y) \ll H$, which is based on the fact that the alongshore variation is usually much smaller than the total depth H for the shallow shelf off the New Jersey coast as shown in Plate 1d. As the study is to focus on the alongshore variations of upwell fronts, for simplicity, only alongshore variations in depth are allowed.

Using xyz as Cartesian coordinates with the z axis pointing vertically upward and the xy plane occupying the undisturbed water surface, the horizontal momentum equations can then be written in the form

$$u_t + \mathbf{v}\cdot\nabla u - fv = -\frac{P_x}{\rho_0} + \frac{\partial}{\partial z}K\frac{\partial u}{\partial z} \tag{1}$$

$$v_t + \mathbf{v}\cdot\nabla v + fu = -\frac{P_y}{\rho_0} + \frac{\partial}{\partial z}K\frac{\partial v}{\partial z}. \tag{2}$$

The approximated hydrostatic pressure is

$$P_z = -\rho g. \tag{3}$$

The density equation is written

$$\rho_t + \mathbf{v}\cdot\nabla\rho + w\bar{\rho}_z = 0. \tag{4}$$

Finally, the continuity equation is

$$u_x + v_y + w_z = 0. \tag{5}$$

Equations (1)–(5) are subject to surface and bottom conditions:

$$K\frac{\partial u}{\partial z} = 0, \qquad K\frac{\partial v}{\partial z} = \tau^y/\rho_0, \qquad w = 0, \qquad z = 0;$$

$$K\frac{\partial u}{\partial z} = C_d u_b, \qquad K\frac{\partial v}{\partial z} = C_d v_b, \qquad w = -vh_y, \tag{6}$$

$$z = -h(y),$$

and to lateral boundary conditions:

$$u = 0 \qquad x = 0$$

$$\frac{\partial}{\partial x} \to 0 \qquad x \to \infty. \tag{7}$$

Here only alongshore (meridional) wind forcing is considered (i.e., $\tau^x = 0$). The first lateral boundary condition assumes that there is no flux through the coastal wall, and the second one assumes that the density and velocity are constant approaching offshore in the x direction. The notation used in these equations is as follows:

u, v, w	the x, y, z components of vector velocity $\mathbf{v}$;
$\rho(x, y, z, t)$	perturbation density;
$\bar{\rho}(z)$	mean vertical stratification;
P	perturbation pressure;
f	Coriolis parameter;
g	acceleration due to gravity;
$h(y)$	bottom topographic variation;
H	maximum depth;
τ^y	alongshore wind stress;
K	eddy viscosity;
C_d	bottom drag coefficient.

Clearly, it is difficult to solve the above three-dimensional system analytically. In sections 2.2–2.4 we will modify the equations such that analytical solutions can be found.

2.2. Parameterization and Forcing

Physically, atmospheric forcing acts on the ocean surface and penetrates to the ocean body through viscosity K, which is parameterized in numerical ocean models. For example, the widely used Mellor-Yamada level-2 turbulent closure scheme [*Mellor and Yamada*, 1974] calculates K by solving equation

$$K\left[\left(\frac{\partial u}{\partial z}\right)^2+\left(\frac{\partial u}{\partial z}\right)^2\right]=\frac{q^3}{c_2 l}-K_H\frac{g}{\rho}\frac{\partial \rho}{\partial z}, \tag{8}$$

where q^2 is the turbulent kinetic energy, l the length scale, c_2 a constant, and K_H the eddy diffusive coefficient. In our case, K_H is assumed to be zero as no vertical diffusion or heat flux is considered.

Another method used to solve the system is by applying a body force to the ocean for the wind stress [e.g., *McCreary and Chao*, 1985; *Boyer et al*., 2000]. In this way the vertical eddy viscosity terms can be replaced by some function, for example,

$$\frac{\partial}{\partial z}K\frac{\partial u}{\partial z}=\frac{\tau^y}{\rho_0 H}F^u(z)\qquad \frac{\partial}{\partial z}K\frac{\partial v}{\partial z}=\frac{\tau^y}{\rho_0 H}F^v(z). \tag{9}$$

Integrating the above equations vertically and using the surface conditions (note $\tau^x = 0$), we have

$$K\frac{\partial u}{\partial z}=0-\frac{\tau^y}{\rho_0 H}\int_z^0 F^u(z)\,dz \tag{10}$$

$$K\frac{\partial v}{\partial z}=\frac{\tau^y}{\rho_0}-\frac{\tau^y}{\rho_0 H}\int_z^0 F^v(z)\,dz. \tag{11}$$

Comparing the above equations with the turbulent closure scheme (8), we notice that in both methods the eddy viscosity coefficient is inversely proportional to some functional form of the vertical shear of the fluid. However, the latter one is not a closed system as the profile needs to be determined. We prefer the latter approach as it allows us to solve the system analytically. Using the bottom drag conditions for (10)–(11), we obtain

$$C_d u_b=0-\frac{\tau^y}{\rho_0 H}\int_{-h}^0 F^u(z)\,dz \tag{12}$$

$$C_d v_b=\frac{\tau^y}{\rho_0}-\frac{\tau^y}{\rho_0 H}\int_{-h}^0 F^v(z)\,dz, \tag{13}$$

where u_b and v_b are bottom velocity. As the meridional wind field is represented by a body force that decays rapidly with depth, the integral of the body foce over the water column should give the wind stress. Therefore, we assume

$$\int_{-H}^0 F^u(z)\,dz=0, \tag{14}$$

$$\int_{-H}^0 F^v(z)\,dz=H. \tag{15}$$

Physically, these assumptions mean that the velocity is zero at the deepest bottom of valleys (no-slip condition) and subject to the bottom drag law at shallower bottom (partial slip condition).

The difficulty is to choose the vertical profile of the body force as the parameterization of subgridscale processes is an unsolved problem. However, observations [e.g., *Price et al*., 1986] have shown that the time-averaged wind-driven velocity has a spiral structure in the upper ocean. On the basis of the physical assumptions and observations we introduce the two functions $F^u(z)$ and $F^v(z)$, called vertical shear friction profiles, as body forces to represent the wind stress as follows:

$$F^u(z)=q_c e^{\cos\,\pi z/H}\left\{\sin\left(\frac{\pi z}{H}+\sin\frac{\pi z}{H}\right)+\alpha\left(1+\frac{z}{H}\right)^2\right\} \tag{16}$$

$$F^v(z)=q_c e^{\cos\,\pi z/H}\left\{\cos\left(\frac{\pi z}{H}+\sin\frac{\pi z}{H}\right)+e^{-1-\cos\,\pi(z/H)}\right\}, \tag{17}$$

where q_c and α are constants chosen to satisfy the bottom conditions (14)–(15).

In fact, the idea of choosing such forms of profiles is inspired by Ekman's solutions. Ekman considered the following simple equations (the Ekman equations):

$$fV_E+K\frac{\partial^2 U_E}{\partial z^2}=0$$

$$-fU_E+K\frac{\partial^2 V_E}{\partial z^2}=0,$$

i.e., Coriolis + friction = 0. He assumed the water to be homogeneous and that there was no slope at the surface. He also assumed an infinite ocean to avoid the complications associated with the lateral friction at the boundaries and the diversion of the flow there. His solutions to the problem are

$$U_E=V_0 e^{\pi z/D_E}\cos\left(\frac{\pi}{4}+\frac{\pi z}{D_E}\right)$$

$$V_E=V_0 e^{\pi z/D_E}\sin\left(\frac{\pi}{4}+\frac{\pi z}{D_E}\right),$$

where $V_0 = 2\pi\tau^y/\mathrm{D_E}\rho\mathrm{f}$ and $D_E = \pi\mathrm{2K/f}$ are the total Ekman surface current and the Ekman depth, respectively. Comparing the Ekman solutions V_E and U_E with $F^u(z)$ and $F^v(z)$ in (16)–(17), we can see the similarity of these two sets of functions (note $\pi z/D_E \simeq \sin\,\pi z/H$). Actually, these two functions $F^u(z)$ and $F^v(z)$ have a very similar vertical profile of the Ekman spiral (see Figure 1); therefore an Ekman flux is qualitatively parameterized into our model. The main purpose of choosing the two functional forms is that they make sense physically and the resulting system can be solved analytically.

It should be noted that the differences between our model and that by *Pedlosky* [1978a, 1978b] and *Killworth* [1978] are mainly the treatment of the wind forcing and the coastal boundary conditions. A schematic view of these two models is given in Figure 2. As we mentioned in section 1, the forcing by *Pedlosky* [1978a, 1978b] and *Killworth* [1978] is represented by a delta function sink of fluid at the coast as the wall condition, i.e., $u = -\tau^y f^{-1}\delta(z)$ at $x = 0$. This assumption does not allow inclusion of the surface Ekman layer in the model. In our case the forcing is parameterized by a body force in the momentum equations, and the coastal wall condition is replaced by $u = 0$ (no flux through the wall) at $x = 0$, which are consistent with reality. This extension allows the model to be

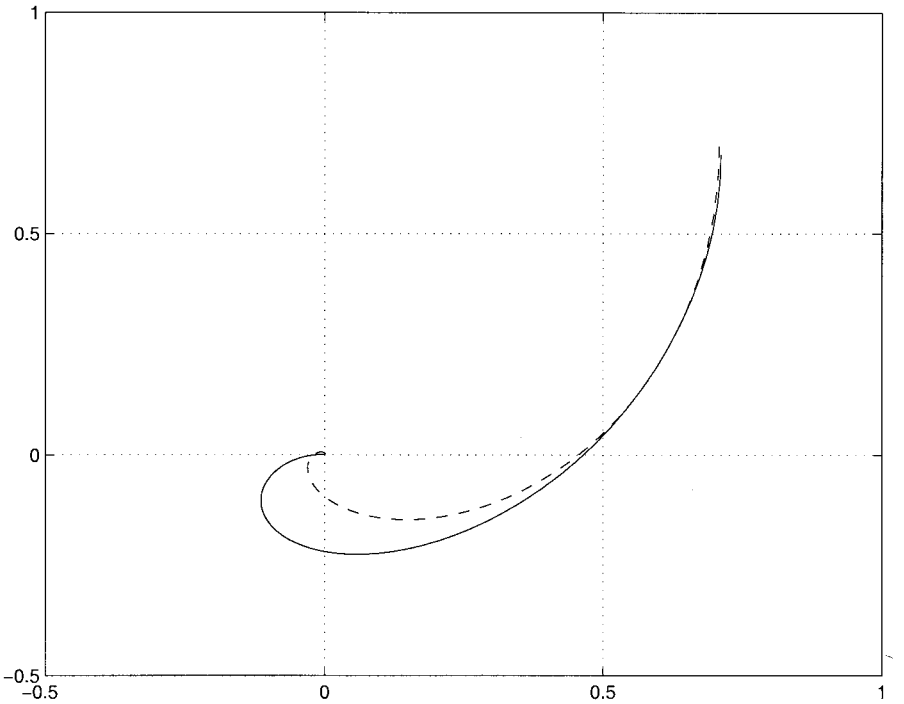

Figure 1. The dashed line is an Ekman spiral with the Ekman depth $D_E = 0.5H$ [*Pond and Pickard*, 1983], and the solid line is the trajectory $(F^v(z), F^u(z))$ used for the vertical friction profiles with $q_c = 0.25$ and $\alpha = 0.8$. Labels are dimensionless.

applied to shallower shelfs of coastal oceans, such as that off the New Jersey coast.

2.3. Scaling and Approximations

In order to solve (1)–(5) we first transform them to nondimensional form. The characteristic scales for the New Jersey coast can be chosen as follows: for vertical and horizontal length scales, $H \sim 50$ m, $L \sim 50$ km, respectively; for wind stress, $\tau^y \sim 1$ dyn cm^{-2} $= 10^{-1}$ pa; and for the mean stratification, $\bar{\rho}_z \sim 2 \times 10^{-2}$ kg m^{-4}. Dimensionless variables are formed in the following manner:

$$N^2 = -\frac{g\bar{\rho}_z}{\rho_0} \sim 2 \times 10^{-4}\ \mathrm{s}^{-2},$$

$$U = \frac{\tau^y}{\rho_0 f H} \sim 2\ \mathrm{cm\ s}^{-1},$$

$$W = \frac{HU}{L} \sim 2 \times 10^{-3}\ \mathrm{cm\ s}^{-1}, \tag{18}$$

$$T = \frac{L}{NH} \sim 0.7 \times 10^5 s \sim 1\ \mathrm{day},$$

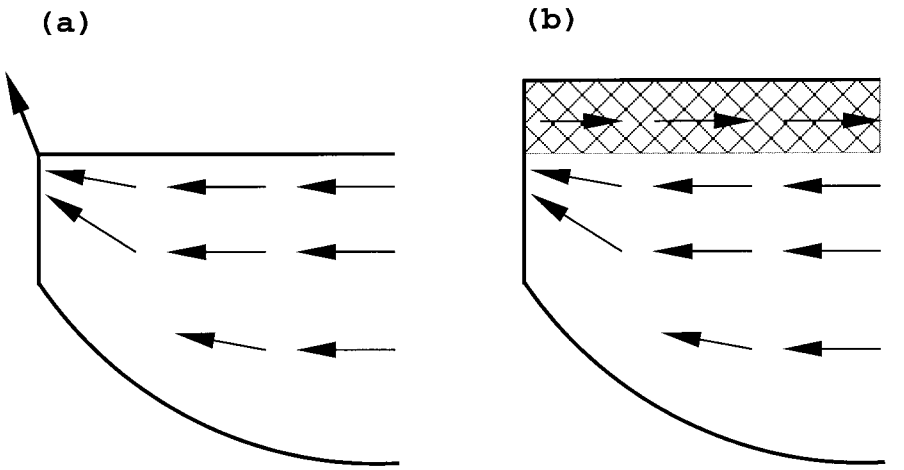

Figure 2. Schematic model structure of (a) *Killworth*'s [1978] model and (b) present model with an Ekman surface layer.

where N is the buoyancy frequency, assumed constant. The equations of motion (1)–(5), combined with the body force (8)–(9), then become

$$\begin{aligned}\sqrt{\gamma}u_t + \varepsilon\mathbf{v}\cdot\nabla u - v &= -P_x + \tau^y F^u(z),\\ \sqrt{\gamma}v_t + \varepsilon\mathbf{v}\cdot\nabla v + u &= -P_y + \tau^y F^v(z),\\ P_z &= -\rho,\\ \sqrt{\gamma}\rho_t + \varepsilon\mathbf{v}\cdot\nabla\rho &= \gamma w,\\ u_x + v_y + w_z &= 0.\end{aligned} \tag{19}$$

Here we have introduced the following dimensionless Rossby and Burger's numbers:

$$\begin{aligned}\varepsilon &= \frac{U}{fL} \sim 4\times 10^{-3}\\ \gamma &= \left(\frac{NH}{fL}\right)^2 \sim 2\times 10^{-2}.\end{aligned} \tag{20}$$

From the above scaling analysis we have the relations

$$\varepsilon \ll \gamma \ll \sqrt{\gamma} \ll 1. \tag{21}$$

Following *Killworth* [1978], terms of $O(\varepsilon)$ are now neglected, thus linearizing the equations. Then we seek approximate expressions for horizontal velocity components u and v in terms of pressure P. Operating on the momentum equations with $\sqrt{\gamma}\,\partial/\partial t$ and combining gives

$$\begin{aligned}(\gamma u_{tt}) + u &= -\sqrt{\gamma}P_{xt} - P_y + \tau^y F^v(z)\\ (\gamma v_{tt}) + v &= -\sqrt{\gamma}P_{yt} + P_x - \tau^y F^u(z).\end{aligned}$$

As the bracketed terms are an order of magnitude smaller than the other terms in the equations, they can be neglected to obtain

$$\begin{aligned}u &= -\sqrt{\gamma}P_{xt} - P_y + \tau^y F^v(z),\\ v &= -\sqrt{\gamma}P_{yt} + P_x - \tau^y F^u(z),\\ w &= -\frac{1}{\sqrt{\gamma}}P_{zt}.\end{aligned} \tag{22}$$

Substituting the above relations into the continuity equation (5), we obtain the pressure equation

$$\frac{\partial}{\partial t}\left[P_{zz} + \gamma(P_{xx} + P_{yy})\right] = 0, \tag{23}$$

provided that τ^y, $F^u(z)$, and $F^v(z)$ are independent of x.

To seek a solution for our problem, we only need to solve the elliptic equation

$$P_{zz} + \gamma(P_{xx} + P_{yy}) = 0 \tag{24}$$

and the corresponding boundary conditions

$$\begin{aligned}P_{zt} &= 0, \qquad z = 0;\\ P_{zt} &= -\sqrt{\gamma}[P_x - \tau^y F^u(z)]B_y, \qquad z = -1 + B(y);\\ \sqrt{\gamma}P_{xt} + P_y &= \tau^y F^v(z), x = 0;\\ P_{xx}, P_{xy} &\to 0, \qquad x \to \infty\end{aligned} \tag{25}$$

It should be pointed out that the offshore boundary condition is different from that of Killworth's model, where $P_x \to 0$ is too strong to guarantee satisfaction of initial $P = 0$ at $t = 0$. Here we relax the remote offshore boundary condition to require the second derivatives of the pressure field to approach zero.

2.4. Coordinates Transformation

In order to solve the above problem we introduce a new east-west coordinate ξ as *Killworth* [1978] did, measured from the coastline to offshore and scaled by the radius of deformation $\sqrt{\gamma}$. Let

$$x = \xi\sqrt{\gamma},$$

then the elliptic equation (24) becomes

$$P_{zz} + P_{\xi\xi} = O(\gamma).$$

By neglecting the term $O(\gamma)$ the equation is simplified to

$$P_{zz} + P_{\xi\xi} = 0. \tag{26}$$

It is convenient to transform (26) into a σ coordinate system $z = (1 - B)\sigma$. Then the system becomes

$$P_{\sigma\sigma} + (1 - B)^2 P_{\xi\xi} = 0, \tag{27}$$

and the corresponding boundary conditions become

$$\begin{aligned}P_{\sigma t} &= 0, \qquad \sigma = 0;\\ P_{\sigma t} &= -P_\xi B_y, \qquad \sigma = -1;\\ P_{\xi t} + P_y &= \tau^y F^u - \sigma B_y P_\sigma, \xi = 0;\\ P_{\xi\xi}, P_{\xi y} &\to 0, \qquad \xi \to \infty\end{aligned} \tag{28}$$

In section 3 we will solve the above problem for pressure and then derive the velocity and density fields.

3. Theoretical Solutions

In this section we use the topographic perturbation method to solve the elliptic boundary condition problem as given by (27)–(28). By the natural assumption that the topographic variation B is small compared with the mean depth we can use the perturbation method as shown by *Killworth* [1978].

In our problem we assume $B(y) = b(y)\delta$, where δ is a small parameter and $b(y) = O(1)$. Then we expand the pressure in a power series in the topography as

$$P = P_0 + P_1\delta + O(\delta^2), \tag{29}$$

where P_0 and P_1 are the zero- and first-order approximation of the pressure, respectively. Similarly, we expand the vertical shear stress function in a Taylor series as

$$F(z) = F(\sigma - \delta b\sigma) = F(\sigma) - \delta b\sigma F_\sigma(\sigma) + O(\delta^2). \tag{30}$$

3.1. Flat Bottom Solution

Inserting the expansions (29)–(30) into the given problem (27)–(28), we first obtain the flat-bottom (zero-order approximation) problem:

$$P_{0\sigma\sigma} + P_{0\xi\xi} = 0 \tag{31}$$

with boundary conditions

$$\begin{aligned}P_{0\sigma t} &= 0, \qquad \sigma = 0, -1;\\ P_{0\xi t} + P_{0y} &= \tau^y F^v(\sigma), \xi = 0;\\ P_{0\xi\xi}, P_{0\xi y} &\to 0, \qquad \xi \to \infty.\end{aligned} \tag{32}$$

The flat-bottom problem is solved in Appendix A and has the form

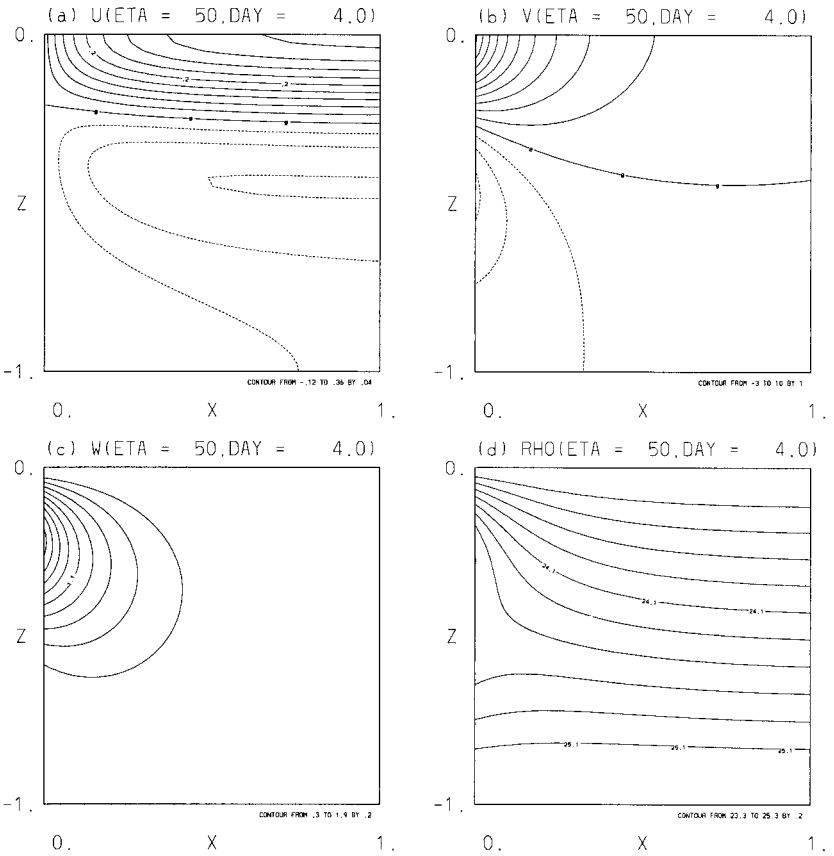

Figure 3. Contours of cross section of flat-bottom solution at $t = 4$ with upwelling favorable wind: (a) cross-shore velocity u, where solid and dashed lines represent offshore and onshore flow, respectively; (b) alongshore velocity v, where solid and dashed lines represent north and south flow, respectively; (c) vertical velocity w; and (d) density ρ. Units are dimensionless.

$$P_0 = \tau^y q_0 y - t\tau^y \Phi(\xi, \sigma), \tag{33}$$

where Φ is defined as

$$\Phi(\xi, \sigma) = \frac{1}{\pi} e^{e^{-\pi\xi}\cos\pi\sigma} \cos(e^{-\pi\xi}\sin\pi\sigma). \tag{34}$$

Using the functions introduced in Appendix A, the flat-bottom solution can be written as

$$u_0 = \tau^y q(\sigma) + \tau^y \Phi_\xi, \tag{35}$$

$$v_0 = -\frac{t\tau^y}{\sqrt{\gamma}} \Phi_\xi - \tau^y F^u(\sigma), \tag{36}$$

$$w_0 = \frac{\tau^y}{\sqrt{\gamma}} \Psi_\xi, \tag{37}$$

$$\rho_0 = \rho(t = 0) + t\tau^y \Psi_\xi, \tag{38}$$

where the subscript 0 indicates the zero-order approximation, i.e., no topographic variation effect. The flat-bottom upwelling solutions at time unit 4 are given in Figure 3. From Figure 3a we can see that the wind-induced Ekman transport in the surface layer (solid lines) is away from the coast and an onshore movement of water (dashed lines) occurs at some depth below the surface. The alongshore flow in Figure 3b shows a surface coastal jet (solid lines) following the wind direction to the north and a returning undercurrent (dashed lines) below it. The undercurrent is much weaker than the surface jet. The mechanism generating the undercurrent is explained by *McCreary and Chao* [1985]. They believe that the undercurrent is induced by an alongshore pressure gradient field established by the surface forcing of wind stress. Our solution clearly confirmed their conclusion, as the first term in the right-hand-side of (33) is the alongshore pressure caused by a southerly wind. This term represents a southward pressure gradient $\tau^y q_0$ that drives the undercurrent. Figure 3c shows that upwelling occurs near the coast to preserve continuity. As expected, the isopycnals slope upward toward the coast (Figure 3d), indicating transport of cold bottom water to the surface. Below, the isopycnals slope downward toward the coast, which agrees qualitatively with the features observed by CTD data off New Jersey (Plates 1a–1c).

Comparing these results with those given by *Pedlosky* [1978a, 1978b] and *Killworth* [1978], the most striking features are the existence of the classical Ekman surface offshore flow and the compensating onshore flow at depth. Other features are the isopycnals sloping downward toward the coast at depth, which are consistent with a nearly geostrophically balanced poleward undercurrent in the interior but are not seen in Pedlosky and Killworth's results. The features in Figure 3d near the coast, where the upward isopycnals do not intersect with the sea surface, are a consequence of the rigid surface assumption's ignoring the sloped sea surface induced by the winds. Never-

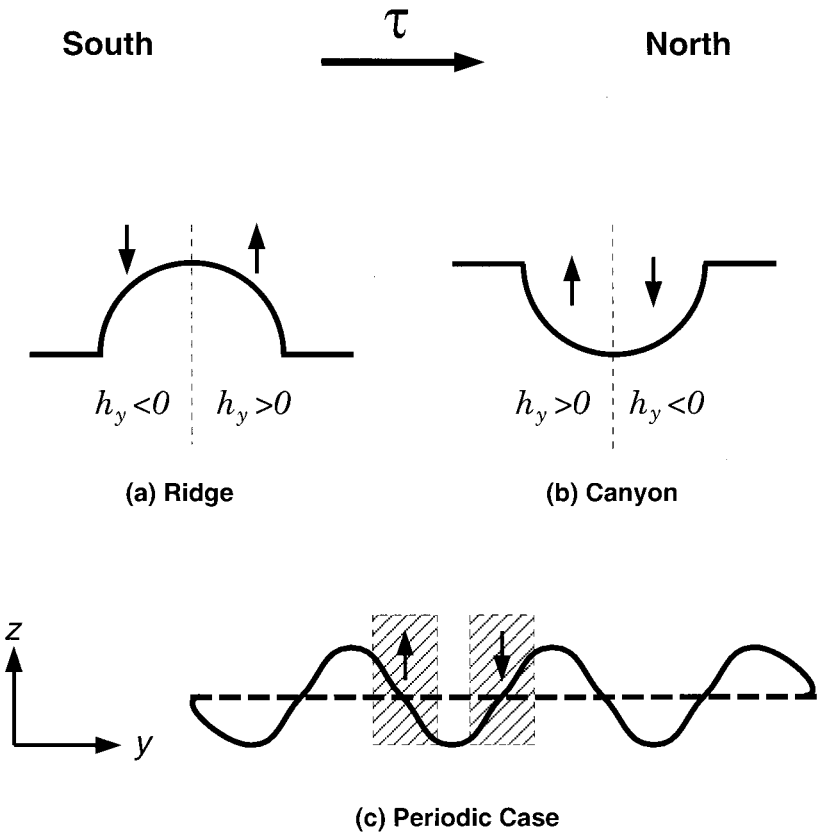

Figure 4. Schematic alongshore sections of topography: (a) a ridge case, (b) a canyon case, and (c) a periodic bottom topography, where the heavy dashed line is its mean topography and the shaded areas are the interval of $[l_1, l_2]$. Arrows represent upwelling or downwelling tendency near the bottom.

theless, the overall structure of the simple solutions is consistent with known upwelling features [*Brink*, 1983].

3.2. Perturbation Solution

With the zero-order approximation solution given by (33) we can derive the first-order topographic perturbation problem from (27)–(28) and (29)–(30) as

$$P_{1\sigma\sigma} + P_{1\xi\xi} = 2b(y)P_{0\xi\xi} \tag{39}$$

with boundary conditions

$$\begin{array}{ll} P_{1\sigma t} = 0, & \sigma = 0; \\ P_{1\sigma t} = -b_y P_{0\xi}, & \sigma = -1; \\ P_{1\xi t} + P_{1y} = -\tau^y b\sigma F'(\sigma) - b_y \sigma P_{0\xi}, & \xi = 0; \\ P_{1\xi\xi}, P_{1\xi y} \to 0, & \xi \to \infty. \end{array} \tag{40}$$

The perturbation solution to this problem is solved in Appendix B and has the form

$$P_1 = -\frac{t^2}{2}\tau^y b_y F_2(\xi, \sigma) - t\tau^y b F_1(\xi, \sigma) - \tau^y Q(\xi, \sigma; y, t), \tag{41}$$

where F_1, F_2, and Q are known functions defined in Appendix B. From the pressure the first-order topographic perturbation velocity fields can be derived as

$$u_1 = \frac{t^2}{2}\tau^y b_{yy} F_2(\xi, \sigma) + \tau^y b[\xi\Phi_{\xi\xi} + \sigma\Psi_{\xi\xi}(0, \sigma) + c_0 - G(\xi, \sigma)], \tag{42}$$

$$v_1 = \frac{\tau^y}{\sqrt{\gamma}}\left[t b_{yy} F_2(\xi, \sigma)\gamma + b_y(F_1 + \sigma\Psi_\xi)\gamma + Q_{yt}\gamma - \frac{t^2}{2} b_y F_{2\xi} - t b F_{1\xi} - Q_\xi \right], \tag{43}$$

$$w_1 = \frac{\tau^y}{\sqrt{\gamma}}[t b_y F_{2\sigma} + b(F_{1\sigma} + \Psi_\xi) + Q_{\sigma t}], \tag{44}$$

where Q_ξ, Q_{yt}, and $Q_{\sigma t}$ are

$$Q_\xi = -\sum_{n=1}^{\infty} q_n n\pi \int_y^{y+t/n\pi} b(\eta)\, d\eta\, e^{-n\pi\xi} \cos n\pi\sigma,$$

$$Q_{yt} = \sum_{n=1}^{\infty} q_n \frac{1}{n\pi} b_y\left(y + \frac{1}{n\pi}\right) e^{-n\pi\xi} \cos n\pi\sigma,$$

$$Q_{\sigma t} = -\sum_{n=1}^{\infty} q_n b\left(y + \frac{1}{n\pi}\right) e^{-n\pi\xi} \sin n\pi\sigma.$$

Similarly, we can derive the perturbation density as

$$\rho_1 = \frac{t^2}{2}\tau^y b_y F_{2\sigma}(\xi, \sigma) + t\tau^y b F_{1\sigma}(\xi, \sigma) + \tau^y Q_\sigma(\xi, \sigma; y, t). \tag{45}$$

3.3. Bottom Structure

Before going into the three-dimensional structure of the perturbation solution we first examine the bottom vertical ve-

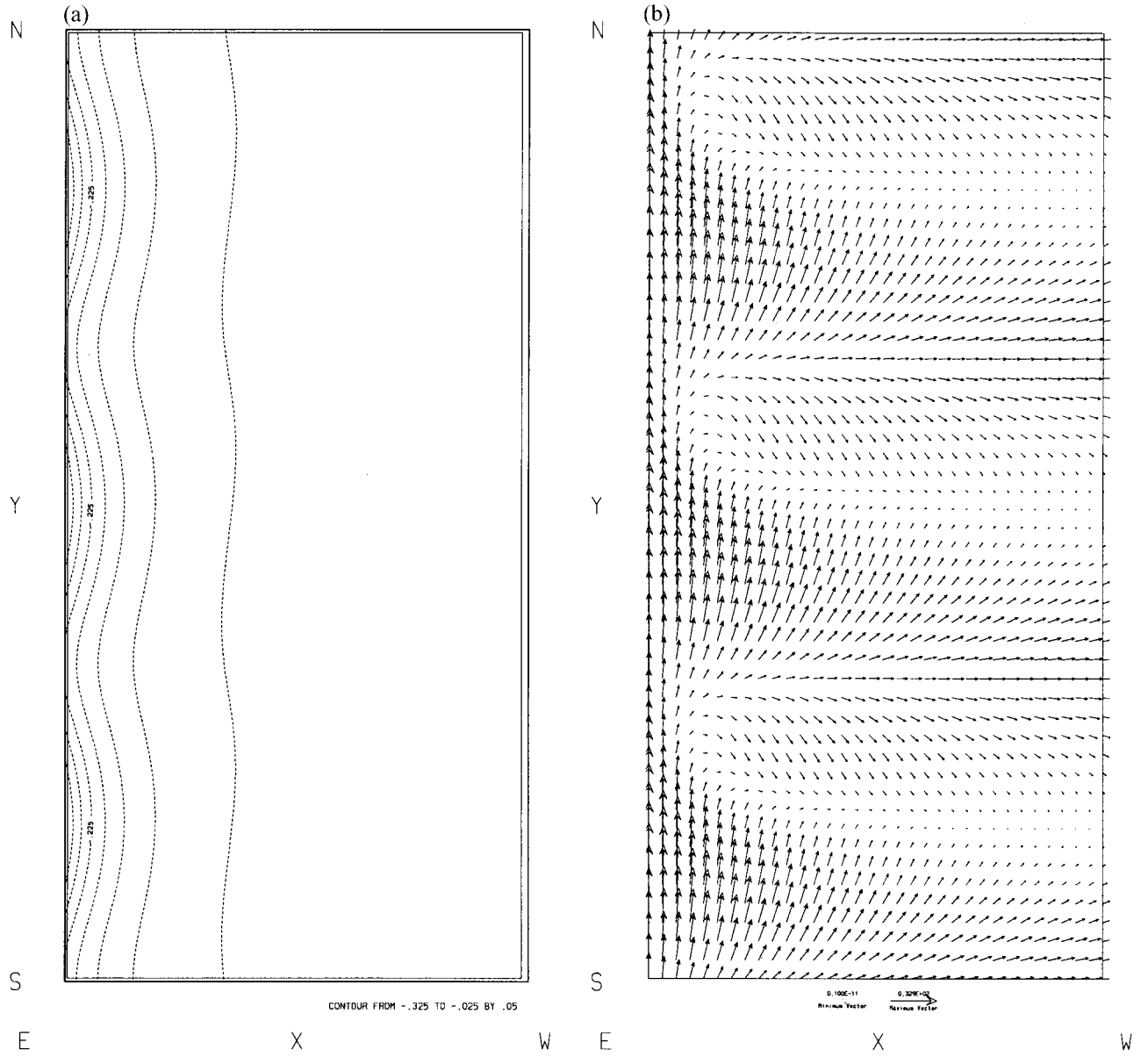

Figure 5. (a) Near-surface perturbation density and (b) velocity. Three upwelling centers are formed, and each of them is located on the north side of a topographic high. Dashed lines indicate decreased temperature (increased density).

locity. The pattern of the upwelling perturbation on the bottom can be predicted from the bottom boundary condition (7) or from the solution w_1. Noting that $h_y = -b_y\delta$, the vertical velocity near the bottom can be written as

$$w_b = -h_y v_0 = \frac{t\tau^y}{\sqrt{\gamma}} h_y e^{-\pi\xi} e^{-e^{-\pi\xi}}, \tag{46}$$

on $\sigma = -1$ as $F_{1\sigma} + \Psi_\xi$ and $Q_{\sigma t}$ vanish and $F_{2\sigma} = -\Phi_\xi$ on the bottom. The sign of h_y determines the upwelling or downwelling on the bottom layer. For example, in case of a ridge, there will be upwelling induced on the downside ($h_y > 0$) of the ridge and downwelling induced on the upside ($h_y < 0$) of the ridge. This corresponds to a tendency for more bottom water to be upwelled to the surface on the north side of the ridge than on the south side of the ridge. Similar arguments apply to a canyon case. Figure 4 shows the schematic structures of the several cases of varying bottom topography. These results are consistent with the observations and the modeling results of *Glenn et al.* [1996].

3.4. Full Solution

The full solutions to problems (1)–(7) have the form

$$u = u_0 + u_1\delta + O(\delta^2), \tag{47}$$

where u_0 is the basic flow given in (35) and u_1 is the topographic perturbation flow given in (42). A value of $\delta = 0.2$ is used in the following calculations. The third term is about two magnitudes smaller than the leading term and is not pursued here. Similar solutions can be derived for v, w, and ρ.

In the following we calculate the full solutions with an along-

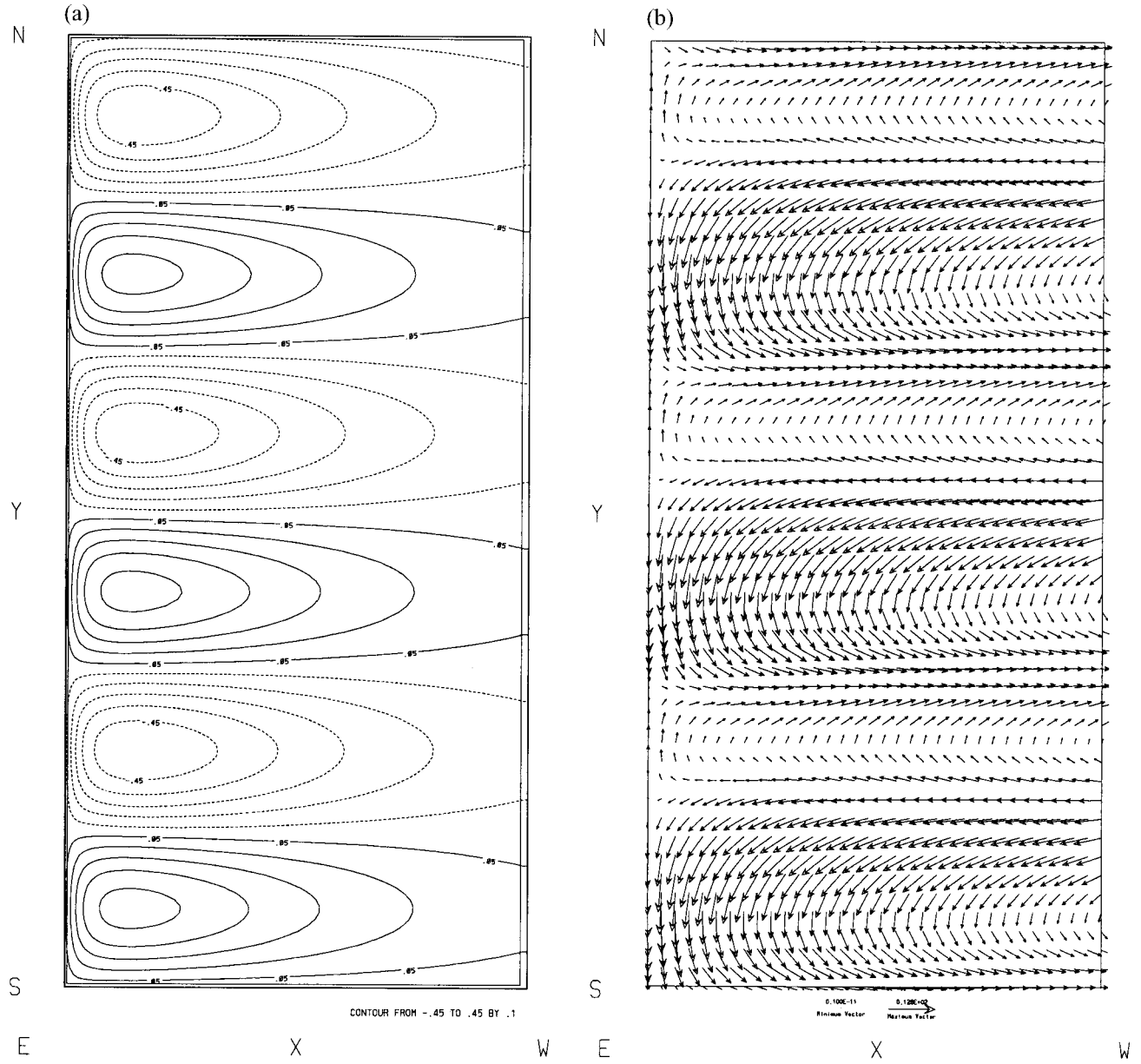

Figure 6. (a) Near-bottom perturbation density and (b) velocity. The bottom temperature field shows enhanced upwelling on the downslope side and downwelling on the upslope side. The velocity field shows the exchange of water masses between coastal and deep oceans.

shore-varying bathymetry $b(y) = 1 - \cos(6\pi y)$. This bathymetry represents the three topographic highs observed along the southern New Jersey shore spaced ~50 km apart in the alongshore direction (see Plate 1d). We plot the near-surface perturbation density and velocity fields in Figure 5. Three upwelling centers are formed and located on the northern sides of these topographic highs, and each corresponds to a strong offshore transport induced by the winds. These features agree with the observations given in Plates 1a–1c. Figure 6 gives the near-bottom perturbation density and velocity field. They show that the exchange of water masses between coastal and deep oceans is characterized in a manner of more deep water transporting onshore near ridges and more coastal water returning back to deep oceans along canyons. The undercurrent is not necessarily continuous, and it is enhanced over the downslope sides of the topographic highs. These features are confirmed in the early modeling results of *Peffley and O'Brien* [1976].

Figure 7 gives the alongshore section of vertical velocity and density at $x = 0.2$ from the coastline. The vertical velocity shows an enhanced upwelling on the northern sides of the topographic highs and a weakened upwelling on the other sides as we expected from the bottom condition (46). The density section Figure 7b shows cold bottom water is upwelled to the surface from northern sides rather than from the south.

To understand further the effects of the topography, we plot two cross-shore sections of the full solution in Figure 8 at a shallow location and in Figure 9 at a deep location. Comparing with the flat-bottom case (Figure 3), we can see that onshore flow and vertical upwelling are enhanced while the undercurrent is weakened near shallow locations (Figure 8). These situations are reversed near deeper locations (Figure 9).

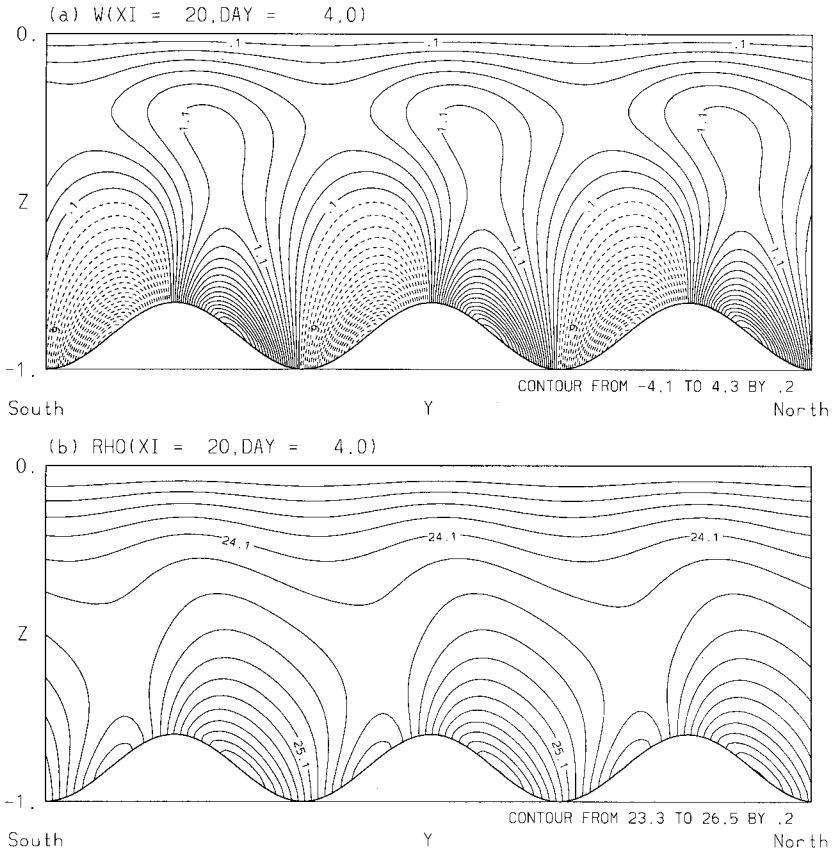

Figure 7. Alongshore section of (a) vertical velocity and (b) density. These results show the upwelling of bottom waters from north sides of the topographic highs.

3.5. Topographically Trapped Kelvin Waves

In the solutions of (42)–(44) the terms Q_{yt}, Q_{ξ}, and $Q_{\sigma t}$ are the components of a topographically trapped Kelvin wave. These terms are boundary phenomenon in the sense that the oscillations are large near the coast and decay away from it because of the factors $e^{-n\pi\xi}$. For example, $\tau^y/\gamma\ (Q_{yt}\gamma - Q_{\xi})$ and $\tau^y/\gamma\ Q_{\sigma t}$ are the Kelvin wave terms of v_1 and w_1, respectively. In addition, the waves propagate forward with the boundary on the right (to the south in the east coast as $y + t/n\pi = c$) independent of along-coast wind direction. As the rigid surface assumption, these waves are internal Kelvin waves with the internal radius of deformation $\lambda_i = \gamma/n\pi$, where $\gamma = NH/fL$. Clearly, each mode of the waves travels in the shape of the bottom topography as shown by the presence of the factors $b(y + t/n\pi)$ in the solutions.

Killworth [1978] examined the Kelvin waves and their energy scattering in great detail. We find that the effects of the Kelvin waves on the full solutions are insignificant; that is, the wave terms are relatively small when compared to other terms in the solutions. In Figure 10 we plot the wave terms of vertical velocity and their effects on the initial density after $t = 4$. We note that the Kelvin waves propagate along the coast to the south, but their magnitude is much smaller than the total value (Figure 7a). Similarly, from the density plots we can see that their influences on the density variations are also very small.

3.6. Upwelling Conservation Theorem

So far we have demonstrated that the alongshore variation of topography plays a role in the varying upwelling fronts. To understand the physical mechanism of the upwelling system, we focus on the effects of the alongshore topography on the volume transport induced by the wind forcing. The volume transport is often used as an alternative to the mass transport because variations of density are small.

For simplicity, we assume $b(y + L) = b(y)$; that is, the north and south sections of the topography are the same, as shown schematically in Figure 4, where L is the length of the coastal ocean segment. The total vertical transport along the coast can be written as (note, only perturbation W_1 is used)

$$M_v = \int_0^L w_1\, dy$$

$$= \frac{\tau^y}{\sqrt{\gamma}}\bar{b}L\left(F_{1\sigma} + \Phi_{\xi} - \sum_{n=1}^{\infty} q_n e^{-n\pi\xi}\sin n\pi\sigma\right), \tag{48}$$

where the alongshore mean topography is $\bar{b} = 1/L \int_0^L b(y)\, dy$ and the change of the transport with respect to time is

$$\frac{\partial}{\partial t} M_v = 0. \tag{49}$$

This means that the total amount of upwelled water is independent of time (conserved) and is also independent of variations in bottom topography. In fact, (48) shows that it is equal to the flat-bottom case (or equal to the case of its alongshore mean topography). Therefore we have the first conclusion, the

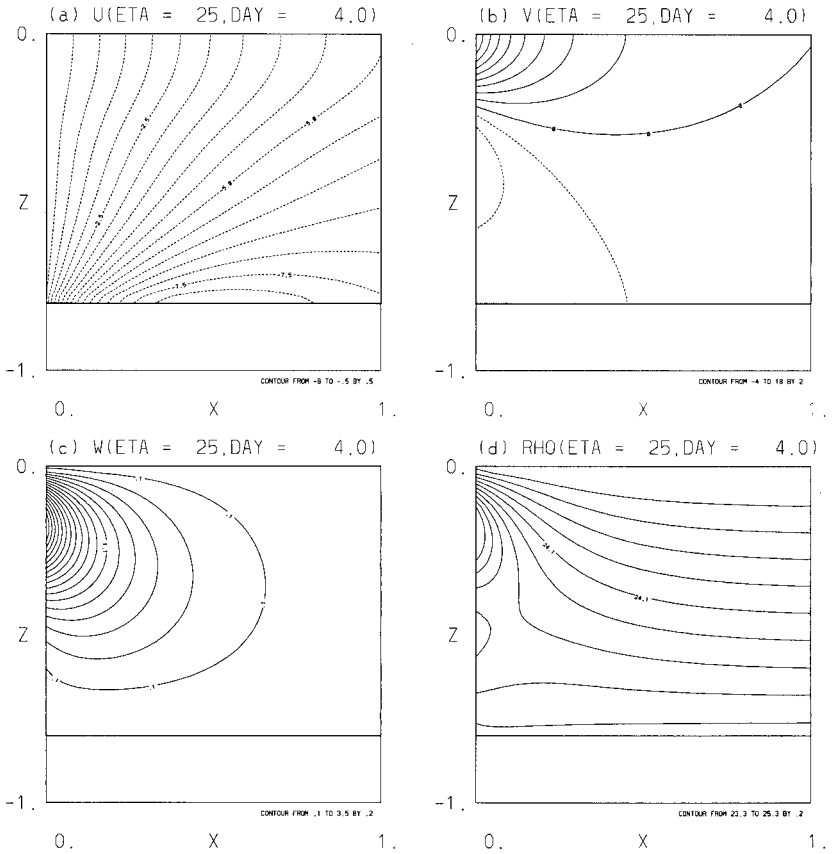

Figure 8. Cross section of the full solution at $t = 4$ along shallower location: (a) cross-shore velocity u, where solid and dashed lines represent offshore and onshore flow, respectively; (b) alongshore velocity v, where solid and dashed lines represent north and south flow, respectively; (c) vertical velocity w; and (d) density ρ.

total upwelling theorem: the total vertical transport is conserved no matter how the topography varies.

Furthermore, we consider a portion (an interval) of the segment of the coastal ocean, $[l_1, l_2]$, in which the topography $b_y > 0$ or $b_y < 0$. For example, we consider the portion at the north or south side of a ridge, the shaded regions shown in Figure 4c. The vertical transport within this portion of the ocean can be written as

$$M_{l_1}^{l_2} = \int_{l_1}^{l_2} w_1 \, dy, \tag{50}$$

and its change with respect to time is not zero but is

$$\frac{\partial}{\partial t} M_{l_1}^{l_2} = \frac{\tau^y}{\sqrt{\gamma}} \left\{ [b(l_2) - b(l_1)] F_{2\sigma} - \sum_{n=1}^{\infty} q_n \left[b\left(l_2 + \frac{t}{n\pi} \right) - b\left(l_1 + \frac{t}{n\pi} \right) \right] \frac{1}{n\pi} e^{-n\pi\xi} \sin n\pi\sigma \right\}. \tag{51}$$

There are two terms in the right-hand side; the first term is due to the topographic perturbation flow, and the second is due to the Kelvin waves trapped by the topography. It can be shown that the Kelvin waves are small compared with other components and the first term is dominant. This demonstrates that the sign of $[b(l_2) - b(l_1)]$ determines the sign of $\partial/\partial t \, M_{l_1}^{l_2}$, as $F_{2\sigma}$ is independent of time and alongshore topography. This suggests that the local vertical transport in the portion of the coastal ocean is not conserved; it can be either increased or decreased depending on the underlying topography. Then we have the second conclusion, the local upwelling theorem: the local vertical transport is not conserved; it can be either increased or decreased depending on the underlying topography.

Combining these two conclusions indicates that the topographic variation does not change the total amount of upwelled water but redistributes it in the manner of transporting more cold water offshore on the north side of the topographic highs and inducing warm water onshore on the other sides. As a consequence, upwelling centers are formed along the coast and actually controlled by the local topography. This might explain the observed features in the coastal oceans where tongues of cold upwelling water, projecting in the offshore direction (where $\partial/\partial t \, M_{l_1}^{l_2} > 0$) and interleaved with tongues of warmer water moving toward the coast (where $\partial/\partial t \, M_{l_1}^{l_2} < 0$), result in meandering fronts and eddies. These variations are further complicated by the topographically trapped Kelvin waves.

4. Summary and Conclusions

In this paper we have developed a wind-driven coastal ocean model by using a vertical shear friction profile to represent the Ekman dynamics in the momentum equations. This method allows us to solve the three-dimensional coastal upwelling problem analytically. The solutions are well defined, simple,

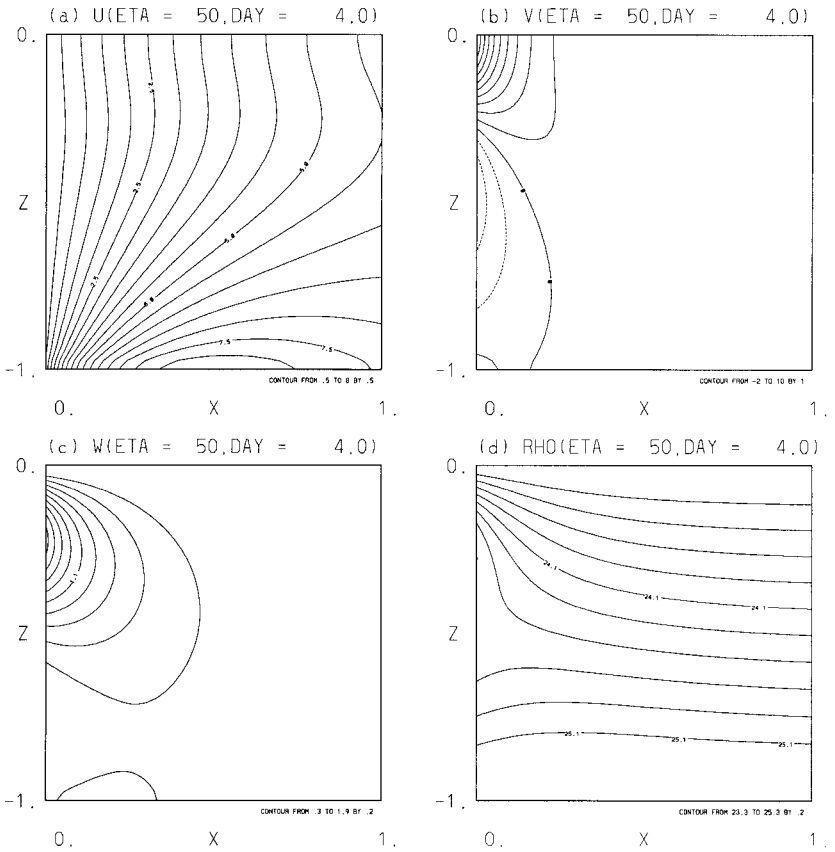

Figure 9. Cross section of the full solution at $t = 4$ along deeper location: (a) cross-shore velocity u, where solid and dashed lines represent offshore and onshore flow, respectively; (b) alongshore velocity v, where solid and dashed lines represent north and south flow, respectively; (c) vertical velocity w; and (d) density ρ.

and consistent with known features of the complicated upwelling system. More importantly, this method clearly reveals the role of topographic variation in the formation of upwelling centers and helps us to understand the physical mechanism of their evolutions in time.

In this theoretical model the upwelling solutions can be decomposed into three components: $\mathbf{V} = \mathbf{V}_0 + \mathbf{V}_t + \mathbf{V}_w$, where $\mathbf{V}_0$, $\mathbf{V}_t$, and $\mathbf{V}_w$ represent basic upwelling, topographic perturbation flow, and topographically trapped Kelvin waves, respectively. The basic upwelling component $\mathbf{V}_0$ is the flat-bottom solution given in (35)–(38) and has a cross-shore circulation structure that is uniform alongshore. This solution can be regarded as the extension of *Pedlosky*'s [1978a, 1978b] two-dimensional theory. Perturbed by the underlying topography, the basic flow is superimposed by the alongshore-varying component $\mathbf{V}_t$, with increasing upwelling near ridges, where upwelled bottom waters are pushed farther offshore near the surface, and decreasing upwelling near valleys, where offshore surface waters are pulled onshore. The existence of the topographic perturbation component indicates that the alongshore topography plays an important role in controlling the formation of upwelling centers as it enhances upwelling at some locations and induces downwelling at others. These circulations are further complicated by the superimposed topographically trapped Kelvin waves $\mathbf{V}_w$, which vary in time and location.

The inclusion of the Ekman layer in the model gives a more complete solution for the wind-driven upwelling system. In the model the water mass is conserved as the upwelled deep waters are transported offshore at the surface layer and unevenly distributed alongshore because of topographic effect, unlike the delta function used by *Pedlosky* [1978a, 1978b] and *Killworth* [1978], which pumps infinite deep waters onshore without transporting them offshore (Figure 2). It is clear that the new model can be used in shallower water regions where the Ekman dynamics is important. In addition, our conservation theorem provides the foundation for understanding the mechanism of the initial formation of varying upwelling fronts. In a related issue, *Barth* [1989] has investigated the linear stability of a coastal upwelling front in the two-layer shallow water limit. His stability theorem suggests that coastal upwelling fronts are likely to be unstable for a wide variety of basic state flow configurations. The fronts can grow two modes of instability with distinctly different horizontal scales [*Barth*, 1994]. However, the instability theorem does not indicate when, how, or where the wavelike features are developed. In fact, our theory does not necessarily contradict the stability theorem as it applies to the initial formation of the fronts before they become unstable. It might be interesting to investigate the connections between the topographic effects and the baroclinic instability theory.

It should be noted that the theory developed here has been simplified by ignoring the effects of, for example, the free surface, varying coastline, and cross-shore slope. As in the rigid surface assumption, other waves (Poincaré, Rossby, etc.) are neglected. This simplification also gives an unrealistic surface

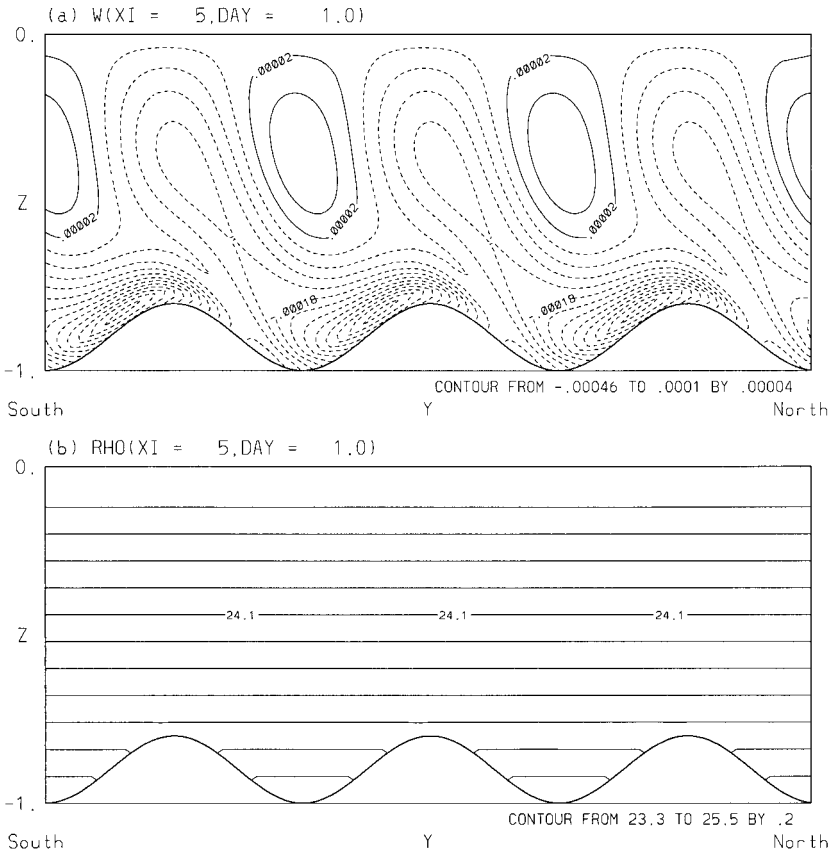

Figure 10. Alongshore section of (a) vertical velocity component due to topographically trapped Kelvin waves (propagating to the south in the east coast) and (b) the final density changed due to the waves at $t = 4$. The signal of the Kelvin waves is clear in Figure 10a, but their influence on the density variations is small in the model.

temperature, as we can see from Figure 3d, where the isopycnals slope upward to the coast but do not intersect the surface. The second simplification, the straight coastline, seems not critical as modeling experiments of *Peffley and O'Brien* [1976] show that topographic variations dominate over coastline irregularities in the upwelling system. Ideally, both alongshore and cross-shore variations of topography should be considered in the model as uh_x is of the same order as vh_y in the bottom boundary condition. The present model did not extend the limitation of ignoring the cross-shore slope by *Killworth* [1978] because of the mathematical difficulties for solving such a complex problem. However, on the basis of the previous studies of *McCreary and Chao* [1985] and *McCreary et al*. [1987] for the California coast the presence of a shelf strengthens the coastal surface jet and weakens the undercurrent but does not significantly affect the qualitative features of the upwelling solutions. In addition, the shelf off the New Jersey coast is broader and more gently sloping than that off the California coast. We believe that the cross-shore slope has less effect on the upwelling off the New Jersey coast than that off the California coast.

Nevertheless, the theoretical model provides important physical insights into the complicated alongshore-varying upwelling fronts. The theory explains what causes the alongshore-varying upwelling fronts, how the water masses are exchanged between the coastal and deep oceans, and what role is played by the topography in controlling the formation of the upwelling centers. The three observed recurrent upwelling centers (Plates 1a–1c) off the New Jersey coast are consistent with the model solutions and are confirmed to be related to the three topographic highs at the locations of Barnegat Inlet, the Mullica River estuary, and Townsend Hereford Inlet, respectively. Clearly, the theory needs further verification from observations and modeling experiments. The importance of the propagation of the topographically trapped Kelvin waves also needs further investigation.

Appendix A: Zero-Order Solution

In order to solve the zero-order approximation problem (31)–(32) for pressure we need the following two trigonometric series:

$$\sum_{n=0}^{\infty} \frac{1}{n!} a^n \cos(nx + y) = e^{a \cos x} \cos(y + a \sin x)$$

$$\sum_{n=0}^{\infty} \frac{1}{n!} a^n \sin(nx + y) = e^{a \cos x} \sin(y + a \sin x).$$

Using these two series, we derive the following three useful functions:

$$\Phi(\xi, \sigma) = \sum_{n=0}^{\infty} k_n e^{-n\pi\xi} \cos n\pi\sigma$$

$$= \frac{1}{\pi} e^{e^{-\pi\xi} \cos \pi\sigma} \cos (e^{-\pi\xi} \sin \pi\sigma), \tag{A1}$$

$$\Psi(\xi, \sigma) = \sum_{n=0}^{\infty} k_n e^{-n\pi\xi} \sin n\pi\sigma = \frac{1}{\pi} e^{e^{-\pi\xi} \cos \pi\sigma} \sin (e^{-\pi\xi} \sin \pi\sigma), \tag{A2}$$

$$q(\sigma) = \sum_{n=1}^{\infty} \frac{1}{(n-1)!} \cos n\pi\sigma = e^{\cos \pi\sigma} \cos (\pi\sigma + \sin \pi\sigma), \tag{A3}$$

where $k_n = 1/\pi n!$ and $q(\sigma)$ has been used to define the vertical shear friction profile. It can be shown that Φ and Ψ are harmonic functions and satisfy relations

$$\Phi_\sigma = \Psi_\xi, \qquad \Psi_\sigma = -\Phi_\xi,$$

$$\Phi_{\sigma\sigma} + \Phi_{\xi\xi} = 0, \qquad \Psi_{\sigma\sigma} + \Psi_{\xi\xi} = 0.$$

With the above introduced functions the zero-order approximation problems (31)–(32) can be solved as

$$P_0 = \tau^y q_0 y - t\tau^y \sum_{n=0}^{\infty} k_n e^{-n\pi\xi} \cos n\pi\sigma, \tag{A4}$$

where $q_0 = -q(-1) = e^{-1}$. Using the function Φ, we have the pressure for the flat-bottom case,

$$P_0 = \tau^y q_0 y - t\tau^y \Phi(\xi, \sigma). \tag{A5}$$

Once the pressure is solved, the velocity and density fields can be derived from it. They can be written in functional form as that given in (35)–(38) or in the explicit form as

$$u_0 = \tau^y [e^{\cos \pi\sigma} \cos (\pi\sigma + \sin \pi\sigma) - e^{-\pi\xi} e^{e^{-\pi\xi} \cos \pi\sigma} \cos (\pi\sigma + e^{-\pi\xi} \sin \pi\sigma)], \tag{A6}$$

$$v_0 = \frac{t\tau^y}{\sqrt{\gamma}} e^{-\pi\xi} e^{e^{-\pi\xi} \cos \pi\sigma} \cos (\pi\sigma + e^{-\pi\xi} \sin \pi\sigma) - \tau^y F^u(\sigma), \tag{A7}$$

$$w_0 = -\frac{\tau^y}{\sqrt{\gamma}} e^{-\pi\xi} e^{e^{-\pi\xi} \cos \pi\sigma} \sin (\pi\sigma + e^{-\pi\xi} \sin \pi\sigma), \tag{A8}$$

$$\rho_0 = \rho(t = 0) - t\tau^y e^{-\pi\xi} e^{e^{-\pi\xi} \cos \pi\sigma} \sin (\pi\sigma + e^{-\pi\xi} \sin \pi\sigma), \tag{A9}$$

where the subscript 0 indicates the zero-order approximation, i.e., no topographic variation effect. Without examining the full structure of the solution we can see its properties near boundaries. With the upwelling favorable wind, $\tau^y > 0$ in the east coast, we have the following features: (1) near sea surface, $\sigma \approx 0$,

$$u_0 \approx \tau^y \{e - e^{-\pi\xi} e^{e^{-\pi\xi}}\} > 0$$

$$v_0 \approx \tau^y \frac{t}{\sqrt{\gamma}} e^{-\pi\xi} e^{e^{-\pi\xi}} + \frac{\tau^y}{e} > 0 \tag{A10}$$

represent a northeastern offshore Ekman transport induced by the wind; (2) near bottom, $\sigma \approx -1$,

$$u_0 \approx \tau^y \{-e^{-1} + e^{-\pi\xi} e^{-e^{-\pi\xi}}\} < 0$$

$$v_0 \approx -\tau^y \frac{t}{\sqrt{\gamma}} e^{-\pi\xi} e^{-e^{-\pi\xi}} < 0 \tag{A11}$$

represent an onshore flow to be unwelled to the surface; and (3) near the coast, $\xi \approx 0$, the vertical velocity

$$w_0 \approx -\frac{\tau^y}{\sqrt{\gamma}} e^{\cos \pi\sigma} \sin (\pi\sigma + \sin \pi\sigma) > 0 \tag{A12}$$

represents an upwelling flow that causes the isopycnals to slope upward to the surface. These features are consistent with observations.

Appendix B. First-Order Solution

The topography perturbation solution to (39)–(40) is assumed to have the form

$$P_1 = -\sigma b(y) P_{0\sigma} + \sum_{n=0}^{\infty} [A_n(y, t) \cdot (\sigma \sin n\pi\sigma + \xi \cos n\pi\sigma) + B_n(y, t) \cos n\pi\sigma] e^{-n\pi\xi}, \tag{B1}$$

with the coefficients A_n and B_n determined by the boundary conditions given by (42). First, it can be seen that the solution satisfies the surface condition $P_{1\sigma} = 0$ (on $\sigma = 0$) and the offshore condition (as $\xi \to \infty$). Then the coefficients A_n and B_n are solved to satisfy the remaining bottom and coastal wall boundary conditions. Substituting the solution into the bottom boundary condition (on $\sigma = -1$) yields

$$\sum_{n=1}^{\infty} (A_{nt} - \tau^y b n \pi k_n - t\tau^y b_y k_n) n\pi (-1)^n e^{-n\pi\xi} = 0, \tag{B2}$$

where k_n is given in Appendix A. The following three coefficients are needed in the calculations:

$$\int_{-1}^{0} \sigma \sin n\pi\sigma \, d\sigma = -\frac{(-1)^n}{n\pi},$$

$$\int_{-1}^{0} \cos n\pi\sigma \cos m\pi\sigma \, d\sigma = \begin{cases} \frac{1}{2} & \text{if} \quad m = n, \\ 0 & \text{if} \quad m \neq n. \end{cases}$$

$$a_{mn} = 2 \int_{-1}^{0} \sigma \sin m\pi\sigma \cos n\pi\sigma \, d\sigma$$

$$= \begin{cases} -\dfrac{1}{2n\pi} & \text{if} \quad m = n, \\ -\dfrac{2m}{(m^2 - n^2)\pi} (-1)^{n+m} & \text{if} \quad m \neq n. \end{cases}$$

As $e^{-n\pi\xi}$ are varying functions in (B2), their coefficients have to vanish. Then we obtain

$$A_n = \frac{t^2}{2} \tau^y b_y k_n + t\tau^y b n \pi k_n, \qquad n \geq 1. \tag{B3}$$

Next we determine B_n by requiring the solution (B1) to satisfy the coastline boundary condition at $\xi = 0$. This yields

$$\sum_{n=1}^{\infty} (A_{ny} - n\pi A_{nt})\sigma \sin n\pi\sigma$$

$$+ \sum_{n=1}^{\infty} (B_{ny} - n\pi B_{nt} + A_{nt}) \cos n\pi\sigma = -A_{0t} - B_{0y}. \quad \text{(B4)}$$

Integrating (B4) from $\sigma = -1$ to 0 gives

$$A_{0t} + B_{0y} = \sum_{n=1}^{\infty} (n\pi A_{nt} - A_{ny}) \int_{-1}^{0} \sigma \sin n\pi\sigma \, d\sigma.$$

From (B3) we have

$$n\pi A_{nt} - A_{ny} = -\frac{t^2}{2} \tau^y b_{yy} k_n + \tau^y b (n\pi)^2 k_n,$$

and we obtain the first two coefficients as

$$A_0(y, t) = 0 \qquad B_0(y, t) = -\frac{t^2}{2} \tau^y b_y c_2 - \tau^y \int_0^y b(\eta)\, d\eta\, c_0, \quad \text{(B5)}$$

where we have defined

$$c_0 = \sum_{n=1}^{\infty} \frac{(-1)^n}{(n-1)!} = -q_0$$

$$c_2 = -\sum_{n=1}^{\infty} \frac{(-1)^n}{n\pi} k_n.$$

Applying the Fourier theorem to (B4), we obtain the following set of hyperbolic equations

$$B_{ny} - n\pi B_{nt} = -A_{nt} - \sum_{m=1}^{\infty} (A_{my} - m\pi A_{mt}) a_{mn}. \quad \text{(B6)}$$

By introducing coefficients

$$r_n = \sum_{m=1}^{\infty} k_m a_{mn}$$

$$g_n = \sum_{m=1}^{\infty} (m\pi)^2 k_m a_{mn}$$

we further simplify (B6) as

$$B_{ny} - n\pi B_{nt} = -\frac{t^2}{2} \tau^y b_{yy} r_n - t\tau^y b_y k_n + \tau^y b (g_n - n\pi k_n) \quad \text{(B7)}$$

with initial condition $B_n(y, 0) = 0$.

This equation has the unique solution

$$B_n(y, t) = -\frac{t^2}{2} \tau^y b_y r_n - t\tau^y b (k_n + n\pi r_n) - \tau^y q_n \int_y^{y + t/n\pi} b(\eta)\, d\eta, \quad \text{(B8)}$$

where

$$q_n = g_n - (2k_n + n\pi r_n) n\pi, \qquad n \geq 1.$$

In order to derive the solution explicitly we introduce the following functions:

$$F_1(\xi, \sigma) = \Phi(\xi, \sigma) - R_\xi(\xi, \sigma) + \xi \Phi_\xi(\xi, \sigma) \quad \text{(B9)}$$

$$F_2(\xi, \sigma) = R(\xi, \sigma) - \sigma\Psi(\xi, \sigma) - \xi\Phi(\xi, \sigma) + c_2, \quad \text{(B10)}$$

where Φ and Ψ are defined in Appendix A, and we define

$$R(\xi, \sigma) = \sum_{n=1}^{\infty} r_n e^{-n\pi\xi} \cos n\pi\sigma, \quad \text{(B11)}$$

$$G(\xi, \sigma) = \sum_{n=1}^{\infty} g_n e^{-n\pi\xi} \cos n\pi\sigma, \quad \text{(B12)}$$

$$Q(\xi, \sigma; y, t) = \sum_{n=1}^{\infty} q_n \int_y^{y + t/n\pi} b(\eta)\, d\eta\, e^{-n\pi\xi} \cos n\pi\sigma$$

$$+ c_0 \int_0^y b(\eta)\, d\eta. \quad \text{(B13)}$$

Finally, we derive the topography perturbation solution as

$$P_1 = -\frac{t^2}{2} \tau^y b_y F_2(\xi, \sigma) - t\tau^y b F_1(\xi, \sigma) - \tau^y Q(\xi, \sigma; y, t). \quad \text{(B14)}$$

It would be useful to point out the strategy used in solving the upwelling system. Most of the functions we have used can have an infinite series form and an analytical form. When solving the equations, it is convenient to use the series form. While calculating the solution, it is easier to use the analytical form. Although it is tedious to solve the above equations, once the solutions are found, it is much easier to verify the solutions in the analytical form. For example, it is straightforward to verify that the perturbation pressure P_1 (B14) satisfies (39). As a matter of convention, we have used lowercase letters for constants and uppercase letters for functions throughout the paper. Finally, we point out the similarities of the infinite series used here and the Chebyshev polynomials used by Semi-spectral Primitive Equation Ocean Model (SPEM) [*Haidvogel et al.*, 1991b]. It would be interesting to compare these two methods in solving the model equations.

Acknowledgments. The research described here was carried out, in part, at the Jet Propulsion Laboratory, California Institute of Technology, under contract with NASA. This work was funded by the Office of Naval Research (N00014-95-1-0457 and N00014-97-1-0797), the National Science Foundation (OCE-95-21102), and the Middle Atlantic Bight National Undersea Research Center (NYB-94-7, MAB-96-10). We thank Mike Crowley for providing Plate 1 and V. Snyder for a careful reading of the manuscript. We are also grateful to J. Klinck and two anonymous reviewers for their suggestions on an earlier version of this paper.

References

Barth, J. A., Stability of a coastal upwelling front, 1, Model development and a stability theorem, *J. Geophys. Res.*, *94*, 10,844–10,856, 1989.

Barth, J. A., Short-wavelength instabilities on coastal jets and fronts, *J. Geophys. Res.*, *99*, 16,095–16,115, 1994.

Boyer, D. L., X. Zhang, and N. Perenne, Laboratory observations of rotating, stratified flow in the vicinity of a submarine canyon, *Dyn. Atmos. Oceans*, *31*, 47–72, 2000.

Brink, K. H., The near-surface dynamics of coastal upwelling, *Prog. Oceanogr*., *12*, 223–257, 1983.

Figley, W., B. Pyle, and B. Halgren, Oxygen depletion and associated benthic mortalities in New York Bight, 1976: Socioeconomic impacts, edited by R. L. Swanson and C. J. Sindermann, *NOAA Prof. Pap. 11*, pp. 315–322, Natl. Oceanic and Atmos. Admin., Silver Spring, Md., 1979.

Glenn, S., M. Crowley, D. Haidvogel, and Y. T. Song, Underwater observatory captures coastal upwelling events off New Jersey, *Eos Trans. AGU*, *77*, 233–236, 1996.

Haidvogel, D. B., A. Beckmann, and K. Hedström, Dynamical simulations of filament formation and evolution in the Coastal Transition Zone, *J. Geophys. Res*., *96*, 15,017–15,040, 1991a.

Haidvogel, D. B., J. L. Wilkin, and R. Young, A semi-spectral primitive equation ocean circulation model using vertical sigma and orthogonal curvilinear horizontal coordinates, *J. Comput. Phys*., *94*, 151–185, 1991b.

Killworth, P. D., Coastal upwelling and Kelvin waves with small longshore topography, *J. Phys. Oceanogr*., *8*, 188–205, 1978.

McCreary, J. P., and S.-Y. Chao, Three-dimensional shelf circulation along an eastern ocean boundary, *J. Mar. Res*., *43*, 13–36, 1985.

McCreary, J. P., P. K. Kundu, and S.-Y. Chao, On the dynamics of the California Current System, *J. Mar. Res*., *45*, 1–32, 1987.

Mellor, G. L., and T. Yamada, A hierarchy of turbulent closure models for planetary layers, *J. Atmos. Sci*., *31*, 1791–1806, 1974.

Moisan, J. R., and E. E. Hofmann, Modeling nutrient and plankton processes in the California coastal transition zone, 1, A time- and depth-dependent model, *J. Geophys. Res*., *101*, 22,664–22,676, 1996.

Moisan, J. R., E. E. Hofmann, and D. B. Haidvogel, Modeling nutrient and plankton processes in the California coastal transition zone, 2, A three-dimensional physical-bio-optical model, *J. Geophys. Res*., *101*, 22,677–22,691, 1996.

Pedlosky, J., An inertial model of steady coastal upwelling, *J. Phys. Oceanogr*., *8*, 171–177, 1978a.

Pedlosky, J., A nonlinear model of the onset of upwelling, *J. Phys. Oceanogr*., *8*, 178–187, 1978b.

Peffley, M. B., and J. J. O'Brien, A three-dimensional simulation of coastal upwelling off Oregon, *J. Phys. Oceanogr*., *6*, 164–180, 1976.

Pond, S., and G. L. Pickard, *Introductory Dynamical Oceanography*, 2nd ed., Pergamon, 329 pp., Tarrytown, N. Y., 1983.

Price, J. F., R. A. Weller, and R. Pinkel, Diurnal cycling: Observations and models of the upper ocean response to diurnal heating, cooling, and wind mixing, *J. Geophys. Res*., *91*, 8411–8427, 1986.

Song, Y. T., and D. B. Haidvogel, Numerical simulations of the CCS under the joint effects of coastal geometry and surface forcing, in *Estuarine and Coastal Modeling*, *Proceedings of the 3rd International Conference, ASCE, Chicago, 1993*, edited by M. L. Spaulding et al., pp. 216–234, Am. Soc. of Civ. Eng., Reston, Va., 1993.

Song, Y. T., and D. B. Haidvogel, A semi-implicit ocean circulation model using a generalized topography-following coordinate system, *J. Comput. Phys*., *115*, 228–244, 1994.

Stoddard, A., J. E. O'Reilly, T. E. Whitledge, T. C. Malone, and J. F. Malone, The application and development of a compatible historical data base for the analysis of water quality management issues in the New York Bight, in *Oceans '86*, vol. 3, pp. 1030–1035, IEEE Press, Piscataway, N. J., 1986.

S. M. Glenn and D. B. Haidvogel, Institute of Marine and Coastal Sciences, Rutgers University, 71 Dudley Road, New Brunswick, NJ 08901.

Y. T. Song, Jet Propulsion Laboratory, California Institute of Technology, 4800 Oak Grove Drive, Pasadena, CA 91109. (song@pacific.jpl.nasa.gov)

(Received January 21, 2000; revised September 7, 2000; accepted October 20, 2000.)